Materials Research Bulletin 64 (2015) 156–162

Contents lists available at ScienceDirect

Materials Research Bulletin

journal homepage: www.elsevier.com/locate/matresbu

Spin polarized state filter based on semiconductor–dielectric–iron–semiconductor multi-nanolayer device

Vladimir I. Makarov [a,*], Igor Khmelinskii [b]

[a] Department of Physics, University of Puerto Rico, Rio Piedras, PO Box 23343, San Juan, PR 00931-3343, USA
[b] Universidade do Algarve, FCT, DQF, and CIQA, 8005-139 Faro, Portugal

ARTICLE INFO

Article history:
Received 10 March 2014
Received in revised form 15 December 2014
Accepted 16 December 2014
Available online 17 December 2014

Keywords:
A. Interfaces
A. Magnetic materials
A. Semiconductor
B. Magnetic properties
D. Spin-density waves

ABSTRACT

Presently we report spin-polarized state transport in semiconductor–dielectric–iron–semiconductor (SDIS) four-nanolayer sandwich devices. The exchange-resonance spectra in such devices are quite specific, differing also from spectra observed earlier in other three-nanolayer devices. The theoretical model developed earlier is extended and used to interpret the available experimental results. A detailed *ab initio* analysis of the magnetic-field dependence of the output magnetic moment is also performed. The model predicts an exchange spectrum comprising a series of peaks, with the spectral structure determined by several factors, discussed in the paper.

Published by Elsevier Ltd.

1. Introduction

Various resonance phenomena are induced in a range of materials by continuous external microwave or radiofrequency electromagnetic fields in the presence of tunable magnetic fields and detected by steady-state resonance techniques or by pulsed microwave or radiofrequency fields in the presence of constant magnetic fields [1]. These include nuclear magnetic resonance, nuclear quadrupole resonance, ferromagnetic resonance, antiferromagnetic resonance, electron spin resonance, etc., observed in ferromagnetic and other materials. All of these resonance effects are strongly dependent on relaxation properties of spin states. The spin-lattice relaxation mechanisms have been studied earlier in detail for metals and metal particles of different size [2–9]. Spin-lattice relaxation in metals may be caused by (i) interaction of spin polarized states with electromagnetic fields induced by fluctuations of electric charge density, and (ii) phonon density, by (iii) SO interactions and (iv) higher-order interactions involving nuclear spin. The spin–spin relaxation processes also affect the spin state dynamics. Therefore, it is very important to develop new methods of theoretical and experimental studies of spin state dynamics in solid samples. The analysis of spin-polarized state dynamics using novel experimental and theoretical approaches is an important fundamental problem. The quantum spin-polarized state filter (QSPSF) device described earlier for metal–dielectric–iron and metal–dielectric–semiconductor devices [10] allows to transfer spin-polarized states between nanolayers of different nature and chemical composition, and measure values of *g*-factor difference between nanolayers and the respective relaxation parameters of the spin-polarized states. Simple interpretations for the formation of spin-polarized states in ferromagnetics, conductors and semiconductors were analyzed [10]. A phenomenological model of spin-polarized state transfer was proposed and discussed [10]. This modeling approach assumes transfer of spin-polarized states between different nanolayers [10]. Experimental measurements of the exchange-resonance spectra in four-layer sandwich structures were also carried out [10]. The presently discussed semiconductor–dielectric–iron–semiconductor (SDIS) structures produce distinct spectra, differing from those obtained earlier for other nanolayer sandwich structures [10]. These spectra are analyzed and interpreted using the earlier and presently developed theoretical models.

2. Experimental

2.1. Device description

The experimental setup used in the current studies has already been described in detail [10]. It was built around the home-made nanosandwich device. This device included a ferrite needle (1) (TPS&TPSA, Power Electronics Technology), with the needle tip 50 μm in diameter made of a stainless-steel capillary filled with

* Corresponding author. Tel.: +1 787 529 2010; fax: +1 787 756 7717.
E-mail address: vmvimakarov@gmail.com (V.I. Makarov).

http://dx.doi.org/10.1016/j.materresbull.2014.12.031
0025-5408/Published by Elsevier Ltd.

ferrite powder suspended in glycerol, and the body 1 mm in diameter. The saturation field and the frequency band for the ferrite are 11–13 kG and $\nu_{H,0} = (1-1.5)\times 10^8$ Hz, respectively. The transmission of the ferrite at frequencies $\nu_H > \nu_{H,0}$ is described by

$$\vartheta(\nu_H) = \vartheta(\nu_{H,0}) e^{-\nu_H - \nu_{H,0}/\nu_{H,0}} \quad (1)$$

A spiral coil of copper wire (0.3 mm wire diameter, 10 turns) was wound on the needle body. The needle tip touched the surface of a Si substrate at the (1 0 0) plane. The opposite surface of the Si substrate, equally (1 0 0), was covered by a sandwich structure, prepared as described separately. A second ferrite item (TPS&TPSA, Power Electronics Technology), with the input surface 10 mm in diameter and the body 1 mm in diameter, contacted the output metal surface by way of a magnetic contact provided by ferrite powder suspended in glycerol (1:1 w/w) (TPS&TPSA, Power Electronics Technology, 25 μm average particle diameter). Copper wire, 0.3 mm in diameter, was wound on the body of the item (10 turns). Note that the same high-frequency ferrite material was used everywhere, rated for up to 100 MHz applications. The entire assembly with the nanosandwich sample was placed into a liquid nitrogen bath (T ≈ 77 K), to reduce noise.

The home-built current generator was controlled via an I/O data acquisition board (PCI-6034 E DAQ, National Instruments), which was programmed in the LABVIEW environment that ran on a Dell PC. The generator fed pulsed currents of up to 10 A into the input coil. The pulse shape was programmed to reproduce the linear function:

$$I_2(t) = \begin{cases} 0, & 0 \le t < t_0 \\ I_0 \times (t - t_0) & t_0 \le t < t_0 + \tau \\ 0, & t_0 + \tau \le t \end{cases} \quad (2)$$

where I_0, t_0 and τ (pulse amplitude, start time and duration) were chosen to obtain the required magnetic field sweep rate. The output coil was connected to a digital oscilloscope (LeCroy; WaveSurfer 432), which collected and averaged the output signal. The I/O DAQ board generated an analog signal that controlled the current generator, and a rectangular TTL pulse 100 ns in duration that triggered the oscilloscope with its rising edge, 100 ns before the start of the analog control signal sweep.

2.2. Multilayer sandwich structure preparation

A detailed description of the device preparation procedure and multilayer sample characterization has been presented earlier [10]. Charge sputtering, vacuum evaporation and laser vapor deposition were used to deposit Fe, SnO_2 and Si, and SiO_2 layers, respectively. The nanolayer deposition procedure has been described earlier [10–12]. The layer thickness was controlled by transmission electron microscopy (TEM) on cross-cut samples, prepared using heavy-ion milling. A typical TEM image of SnO_2 (h_{S1} = 8.0 nm)–SiO_2 (h_d = 8.1 nm)–Fe (h_{Fe} = 7.9 nm)–Si (h_{S2} = 8.4 nm) device is shown in Fig. 1. The four-nanolayer devices were used in the present series of experiments, with the measurements mostly conducted at LN_2 temperature (~77 K).

The exchange resonance spectra and their amplitude dependence on the magnetic field sweep rates were recorded using the same data acquisition system as earlier [10], briefly described above.

3. Results and discussion

We studied the exchange-resonance spectra for a series of four-nanolayer sandwich devices, with semiconductor–dielectric–iron–semiconductor (SDIS) structure. These SDIS devices used the SnO_2 (h_{S1} = 8.0 nm), SiO_2 (h_d = 8.1 nm), Fe (h_{Fe} = 7.9 nm) and Si (h_{S2} = 8.4, 9.1, 9.7, 10.1, 10.8, 11.6, 12.3, 12.8, 13.5 and 14.1 nm) layers, with h_i denoting the respective layer thickness. All of these devices were tested at LN_2 temperatures, using a 50 μm diameter needle tip. The magnetic field sweep rate was 0.684 kG/μs, with the maximum magnetic field of 6.84 kG generated at 10 μs sweep duration. Fig. 2 shows typical experimental exchange resonance spectra obtained presently.

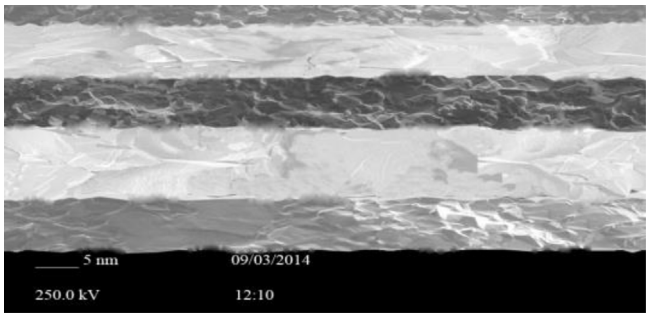

Fig. 1. TEM image of a cross-cut SnO_2 (h_{S1} = 8.0 nm) + SiO_2 (h_d = 8.1 nm) + Fe (h_{Fe} = 7.9 nm) + Si (h_{S2} = 8.4 nm) sandwich structure on a Si substrate.

Fig. 2a demonstrates the complete exchange resonance spectrum recorded within the total sweep range of 0 to 10 μs, while Fig. 2b shows only the lower-field part of the same spectrum recorded at shorter sweep times. Detailed analysis suggests that the spectra may be represented by a superposition of at least four independent spectral components, shown in Fig. 3. These components were extracted as described below.

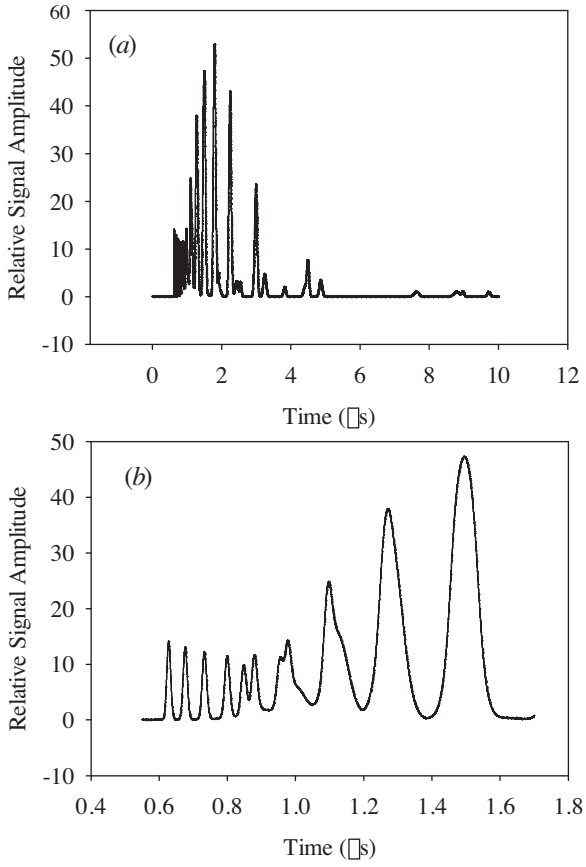

Fig. 2. Output signals of a four-layer (a) SnO_2 (h_{S1} = 8.0 nm), SiO_2 (h_d = 8.1 nm), Fe (h_{Fe} = 7.9 nm) and Si (h_{S2} = 8.4 nm) device presented on the entire available time scale, (b) initial part of the spectrum of (a). The data were recorded at 77 K.

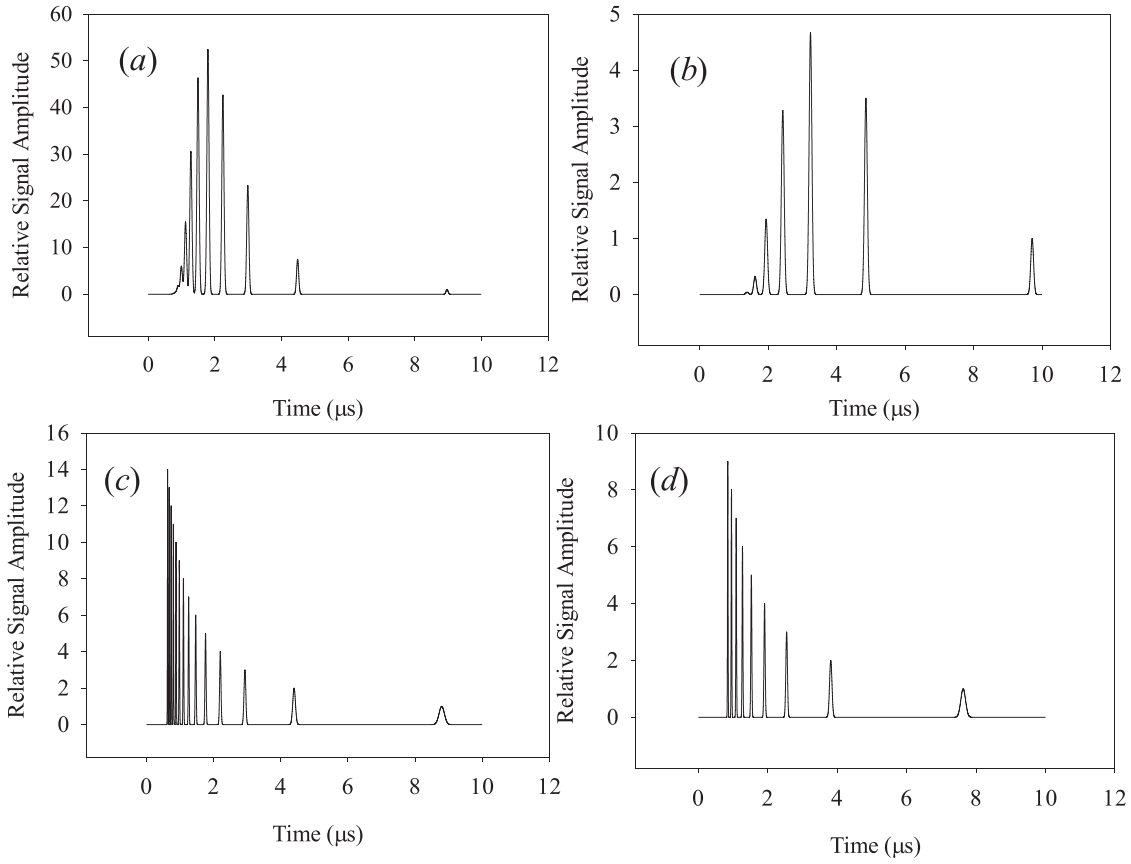

Fig. 3. Spectral components extracted from the experimental spectrum of Fig. 2: (a) low-spin state component (exchange interaction is stronger than spin–spin interaction); (b) low-spin state component; (c) high-spin state component (exchange interaction is weaker than spin–spin interaction); (d) high-spin state component.

Note that the experimental spectra contain discrete lines, some of these containing several superimposed individual contributions. Such composite lines were fitted by a sum of 2 or 3 Lorentz components:

$$I(t) = \frac{A_i}{1 + B_i(t - \tau_i)^2}; \quad i = 1,2\text{or } 1,2,3 \tag{3}$$

where A_i, B_i, τ_i are fitting parameters, while simple lines were represented by a single Lorenz component (3). The entire set of the fitting parameters A_i, B_i and τ_i was analyzed to manually identify sequences of interrelated peaks, which resulted in 4 complete spectral sequences identified. The results are presented in Table 1 and Fig. 3, with the line shapes always described by the function (3).

The structure of the spectral components shown in Fig. 3a, b in different from those of Fig. 3c, d and will be discussed later. For now, we shall only note that we number the spectral lines in each of the components starting from the line located in the highest fields (later in the sweep) and continuing to those appearing in lower fields (earlier in the sweep). We interpret these line numbers M_S as projections of the total system spin on the external field direction [10]. Note also that the spectral components of Fig. 3a, b may be assigned to low-spin states (the exchange interaction is stronger than the spin–spin interaction), while the spectral components of Fig. 3c, d may be assigned to high-spin states (the exchange interaction is weaker than the spin–spin interaction) [10].

We also found that the linewidths in the exchange resonance spectra are significantly dependent of the (last) Si nanolayer thickness. As an illustration, plots of the linewidth for the line number 3 in the spectral components of different samples in function of the thickness of the Si layer are shown in Fig. 4.

The plots of Fig. 4 may be fitted with good accuracy by the function

$$\Delta t = \Delta t_0\left(1 - e^{-h_{S2}/\Delta h}\right) \tag{4}$$

where Δt_0 and Δh are empirical parameters, with the respective values: (a) 0.37, 29; (b) 0.31, 31; (c) 0.43, 28; (d) 0.53, 32, for each of the four components. These results are not discussed presently; we therefore refer the reader to a follow-up paper. In Fig. 4, the plots marked by (a)–(d) correspond to the individual spectral components presented in Fig. 3.

Comparison of the exchange resonance spectra obtained in the present study with those reported earlier for ferromagnetic–dielectric–metal (FDM) three-nanolayer device shows significant differences: the earlier recorded FDM spectra [10] have a regular peak structure–(a) the peak with the maximum intensity is located in the lowest field (the smallest time); (b) the peak intensity decreases with the magnetic field strength; (c) the gaps between the peak maxima increase with the magnetic field strength; (d) the exchange resonance spectra can be described by a single spectral component. However, the presently recorded spectra are more complex, and will be interpreted using the theoretical models developed for SDIS devices.

A detailed theory of electronic gas and magnon waves in metals has been developed earlier, and presented elsewhere [13–15]; however, no detailed treatment had been proposed for nano-layered systems. Therefore, presently we shall limit our

Table 1
Values of the phenomenological parameters: A_i,B_i, τ_i for the four components of the exchange–resonance spin-anticrossing spectra of Fig. 2.

Number	A_i	$(B_i \times 10^3\ \mu s)^{-1}$	$\tau_i \times 10^3\ \mu s$
(a)			
1	4.91	71.74	9131.0
2	24.43	65.76	4565.5
3	48.91	60.70	3043.7
4	55.02	56.36	2282.7
5	39.41	52.67	1826.2
6	19.03	49.32	1521.8
7	6.34	46.42	1304.4
8	1.44	43.84	1141.4
9	0.21	41.53	1014.6
10	0.02	39.46	913.1
(b)			
1	1.03	80.83	9879.1
2	3.60	74.09	4939.2
3	4.81	68.39	3293.0
4	3.37	63.51	2469.8
5	1.38	59.27	1975.8
6	0.33	55.57	1646.5
7	0.04	52.30	1411.3
(c)			
1	0.65	109.11	8973.7
2	1.30	54.82	4486.5
3	1.96	36.34	2991.1
4	2.61	27.25	2243.2
5	3.26	21.80	1794.6
6	3.91	18.17	1495.5
7	4.56	15.57	1281.8
8	5.22	13.63	1121.6
9	5.87	12.11	997.0
10	6.52	10.90	897.3
11	7.17	9.91	815.7
12	7.83	9.08	747.7
13	8.48	8.38	690.2
14	9.13	7.78	640.9
15	9.78	7.27	598.2
16	10.43	6.81	560.8
17	11.09	6.41	527.8
18	11.74	6.06	498.5
19	12.39	5.74	472.3
20	13.04	5.55	448.6
21	13.70	5.19	427.3
22	14.35	4.95	407.9
23	15.00	4.74	390.1
(d)			
1	1.16	121.8	7687.7
2	2.32	60.10	3843.4
3	3.49	40.33	2562.3
4	4.65	30.25	1921.7
5	5.81	24.20	1537.4
6	6.97	20.17	1281.2
7	8.13	17.29	1098.1
8	9.30	15.13	960.9
9	10.46	13.44	854.1

interpretation of the experimental data to the previously proposed empirical model [10].

Note that the exchange resonance effects disappear with increased thickness of the Si layer, becoming unobservable at thicknesses exceeding 1 μm. Therefore, we conclude that such quantum effects are only observable in nanostructured systems.

4. Models and discussion

4.1. Qualitative interpretation of the spectra

The observed effects may be explained qualitatively, if we take into account that metal or semiconductor nanolayer may be described as a 3D system, with a low-density discrete series of electronic states quantized in the z direction normal to the layer, and a high-density quasicontinuum of states quantized in the xy plane (of the layer). We assume that the states located in different nanolayers interact by the exchange mechanism. Note that interactions between quasicontinuum spectra are irrelevant for our present purposes, resulting in classical magnetic momentum transport between nanolayers in presence of an external magnetic field. However, the interactions between discrete spectra of different nanolayers may generate spin anticrossing effects in external magnetic fields, due to differing electron g-factors in the two interacting layers. Noting that the energies of Fermi levels are also different in different nanolayers, we should expect strongly nonequilibrium populations in pairs of spin-polarized states coupled by the exchange interaction. The changes in electron populations resulting from equilibration will be observable via spin anticrossing effects, generated by resonance transport of spin polarization between nanolayers. Next, we shall briefly outline the earlier developed phenomenological theory describing spin anticrossing spectra [10].

4.2. Phenomenological model

A detailed analysis of the phenomenological model has earlier been presented for three-nanolayer systems [10]. The exchange resonance spin-anticrossing phenomena shown in Fig. 2 were considered in the framework of two coupled spin states. As applied to the four-nanolayer device presently discussed, we assign the second level to the combined Fe–Si bilayer, where we have Fe and Si nanolayers in direct contact. The calculated values of the model parameters are presented in Table 2, including ω_0 (cm^{-1}), the zero-field energy gap between the coupled spin-states; f, the relative weight of each of the components of Fig. 3 in the original spectrum of Fig. 2; Δg_{12} is the g-factor difference of the SnO_2 and Fe–Si nanostructures; $\langle V_{12} \rangle$ is the matrix element of exchange interaction coupling the spin-states of interest; γ_1 and γ_2 are widths of the coupled spin-states, dependent on the spin-lattice relaxation rates. Note that typical spin-lattice relaxation times are in the range of 0.1–1.0 μs [14]. This two-coupled-spin-states model corresponds to a selected exchange–interaction anticrossing peak ($S_{S1} = S_{S2} = S$; $\Delta M_S = 0$).

Table 2 shows that the g-factor difference between SnO_2 and Fe–Si nanostructures is ca. 1.7. Note that that the g-factor values for bulk SnO_2 and Si are close to 2, therefore their respective difference as evaluated between bulk materials should be very small. However, we already noted [10] that significant deviations from bulk g-factor values are possible in nanostructures, qualitatively explaining the results obtained. This conclusion is supported by the *ab initio* analysis of the four-nanolayer sandwich devices presented below.

4.3. Ab initio analysis

Exchange interaction and spin-orbital momentum coupling are the quantum phenomena directly responsible for the magnetic properties. The magnetocrystalline anisotropy can be explained using simple quantum statistical models, known as Callen–Callen or Akulov law, as well as the $T^{3/2}$ temperature dependence of magnetization deviation from its 0 K value (Bloch law). However, analytical models are unable to treat complex systems, therefore, numerical calculations are required. The full-Hamiltonian eigenvalue problem may only be solved in a few cases, therefore extra approximations are needed. Numerical analysis of four-layer sandwich systems may be performed using the coupled-cluster theory (CCT) with magnetic phenomena included. Other approximations may also be used in the analysis of the system considered.

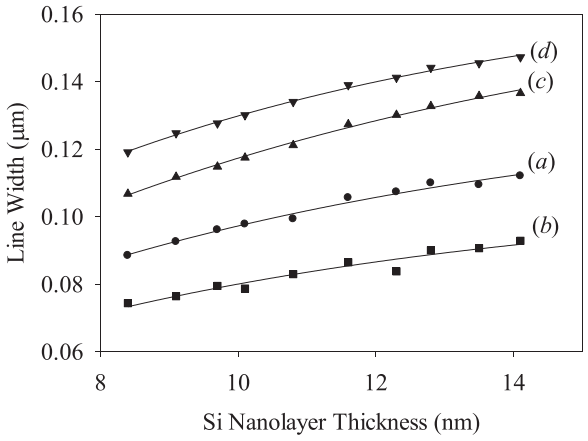

Fig. 4. The Si layer thickness dependences of the linewidths in the four-layer sandwich structure with SnO_2 (h_{S1} = 8.0 nm), SiO_2 (h_d = 8.1 nm) and Fe (h_{Fe} = 7.9 nm) layers; (a)–(d) refer to the respective spectral components of Fig. 3.

Presently we used the CCT and the local electron density approximation (LEDA) and local spin density approximations (LSDA), adding the spin-orbit coupling to the functional in order to calculate magnetic properties of nanolayers. The effective system Hamiltonian included only the magnetic-moment degrees of freedom in each of the nanolayers, and boundary conditions on the layer interfaces. Thus, we used the Hamiltonian in each of the nanolayers in the form [13–16]:

$$\hat{H}^{(X)} = -\sum_{i\neq j}\hat{j}_{ij}^{(X)}\left(m_i^{(X)}\times m_j^{(X)}\right) - \sum_i d_i^{(X,0)}\left(m_i^{(X,z)}\right)^2 - \sum_{i\neq j} d_{ij}^{(X,2)}\left(m_i^{(X,z)}\times m_j^{(X,z)}\right) - \sum_i g_i^{(X,0)}\mu_B\left(m_i^{(X,z)}\times\vec{H}\right) \quad (5)$$

where X = SnO_2, SiO_2, or Fe–Si layer, $d_i^{(X,0)}$ is the single-ion anisotropy, $d_{ij}^{(X,2)}$ is the ion-pair anisotropy and $\hat{j}_{ij}^{(X)}$ is the effective exchange interaction parameter. Here $m_i^{(X)}$ are sublattice elementary cell total spin-orbital angular momenta of the *i-th* electron, H is the external magnetic field strength, and $g_i^{(X,0)}$ is the electron g-factor determined below. Ideally, the input data should include the crystal structure of the Si crystal (the substrate surface), the lattice structure of the SnO_2 nanolayer deposited on the Si substrate, that of the SiO_2 nanolayer deposited on SnO_2 nanolayer, and those of the Fe nanolayer deposited on the SiO_2 nanolayer and the Si nanolayer deposited on the Fe nanolayer [17–21]. To simplify the calculations, we considered the SnO_2–Vacuum–Fe–Si sandwich structure, neglecting the effects of the substrate and the dielectric. The boundary conditions on the layer interfaces are set to minimize the system energy. Note that in the last step of calculations, the elementary cell parameters were fixed. This approximation produced interface "stress" of ca. 0.1–0.3 eV, decreasing exponentially away from the interface. The average magnetic moment of SnO_2 and Si is zero in bulk crystals but not in nanolayers, due to strong coupling between the ground state and the excited states with nonzero multiplicity.

4.4. Computational methods

We used two independent *ab initio* approaches, as outlined below.

The first approach used commercial Gaussian–2000 software package to calculate the wavefunctions. CCT, LEDA and LSDA methods were used with the 6–31G(d) basis set. The total number of atoms (324) in the 2D model of the sandwich structure was distributed between SnO_2 layer ($6\times6\times3$ atoms), Fe layer ($6\times6\times3$ atoms) and the Si layer ($6\times6\times3$ atoms). The SiO_2 layer was represented by a structureless vacuum space with the thickness of $n = h_d/\overline{d}_{SiO_2}$ SiO_2 molecule diameters, where h_d is the real thickness of the dielectric nanolayer, $\overline{d}_{SiO_2}$ being the average diameter of the SiO_2 molecule. We also analyzed a 1D model containing 66 molecules/atoms located along the same axis: 30 SnO_2 molecules that are in contact and separated by an empty space from 36 Fe and 36 Si atoms, which also are in contact. The number of atoms in the 1D model approximately corresponds to the value of layer thickness divided by the respective particle diameter, while the empty space width was chosen to produce correct $n = h_d/\overline{d}_{SiO_2}$, with $\overline{d}_{SiO_2}$ being the SiO_2 molecule diameter. Note that all of the calculations discussed above were additionally repeated using the ROCK CLUSTER software package.

The results of the first step were used as input data for our home-made Fortran code that calculates the magnetic moment in function of the external magnetic field strength using the Hamiltonian (5), where the $g_i^{(X,0)}$ values were calculated in the *j–j* coupling scheme as follows [16]:

$$g_{i,j}^{(X,0)} = \frac{1}{2\left(j_{i,j}^{(X)}\right)^2}\left\{g_{i,l}^{(X,0)}\left[\left(j_{i,j}^{(X)}\right)^2 + \left(l_{i,l}^{(X)}\right)^2 - \left(s_{i,s}^{(X)}\right)^2\right] + g_{i,s}^{(X,0)}\left[\left(j_{i,j}^{(X)}\right)^2 - \left(l_{i,l}^{(X)}\right)^2 + \left(s_{i,s}^{(X)}\right)^2\right]\right\} \quad (6)$$

Here, $g_{i,j}^{(X,0)}$ is the g-factor operator, $g_{i,l}^{(X,0)}$ the orbital angular momentum g-factor, $g_{i,s}^{(X,0)}$ is the spin angular momentum g-factor, $j_{i,j}^{(X)}$ is the total angular momentum, $l_{i,l}^{(X)}$ is the orbital angular momentum, and finally $s_{i,s}^{(X)}$ is the spin angular momentum, all of the *i-th* electron in the nanolayer X.

The discussed approach gives the magnetic field strength dependences of the magnetic moment averaged over the output surface for SnO_2–vacuum–Fe–Si four-nanolayer sandwich device, producing a set of resonances in the same range of the magnetic field values as the experimental exchange resonance spectra. Our home-made FORTRAN code was used for numerical analysis of both Eqs. (5) and (6).

The analysis started with the sets of eigenvalues $\left\{E_k^{(0)}\right\}$ and eigenvectors $\left\{\psi_k^{(0)}\right\}$ obtained using the Gaussian-2000 or the

Table 2
Values of the phenomenological model parameters.

S	ω_0, cm^{-1}	Relative contribution	Δg_{12}	$\langle V_{12}\rangle$, cm^{-1}	γ_1, cm^{-1}	γ_2, cm^{-1}
(a) 12	0.0705	0.31	1.703	1.42×10^{-4}	1.12×10^{-4}	1.31×10^{-4}
(b) 13/2	0.0621	0.20	1.752	1.52×10^{-4}	1.23×10^{-4}	1.24×10^{-4}
(c) 12	0.0808	0.27	1.779	1.49×10^{-4}	1.26×10^{-4}	1.39×10^{-4}
(d) 15/2	0.0726	0.22	1.698	1.63×10^{-4}	1.11×10^{-4}	1.41×10^{-4}

ROCK CLUSTER [22] software, used to calculate the average $V(H) = \Sigma_i g_i^{(X,0)} \mu_B (m_i^{X,z} \times \mathrm{H}^{\rightarrow})$ value for a given magnetic field strength using Eq. (6) and

$$\hat{\mathrm{H}}^{(X)} = -\sum_{i \neq j} \hat{J}_{ij}^{(X)} \left(m_i^{(X)} \times m_j^{(X)} \right) - \sum_i d_i^{(X,0)} \left(m_i^{X,z} \right)^2 - \sum_{i \neq j} d_{ij}^{X,2} \left(m_i^{X,z} \times m_j^{X,z} \right) \quad (7)$$

This was repeated for different values of the magnetic field strength, testing the derivative $d\langle V(H)\rangle/dH$ in order to find the extremum values H_{ext} of $\langle V(H)\rangle$. The magnetic moment values corresponding to these extremums were calculated using

$$\mu(H_{ext}) = \frac{\langle V(H_{ext})\rangle}{H_{ext}}$$

The results are shown in Table 3, where the positions of resonances and values of the output magnetic moments (proportional to the line intensity) are listed. We see that the calculated peaks are in the same range as the experimentally observed anticrossing resonances, although no quantitative agreement could be achieved. Note that 0.684 kG/μs sweep rate should be used to transform the sweep time scale into the magnetic field scale.

Note that we are considering quantum phenomena due to spin–state anticrossing effects induced by exchange interaction between different layers. This interaction only exists when the total spin angular momentum and its projection on the magnetic field direction are the same for the two coupled states.

However, the second theoretical approach gave better results. This approach has been proposed earlier [23] and uses first-principle pseudopotential method within the spin density functional theory. Ultrasoft atomic pseudopotentials [24] and the generalized gradient approximation (GGA) [20] for the exchange and correlation potentials were used within the Quantum-ESPRESSO package [25]. We analyzed the same 4-layer structure, where the Si substrate was neglected. Namely, a Γ-centered $6 \times 6 \times 9$ k mesh was used to sample the irreducible Brilouin zone in the Monkhorst–Pack scheme [26]. To improve the analysis accuracy so that neighboring exchange anticrossing peaks become resolved, the Methfessel-Paxton technique was adopted with a smearing width of 0.001 Ry [27,28]. Smearing procedure was used because of the Fe nanolayer present. Convergence better than 5×10^{-6} eV was achieved for the total energy. We used published bulk crystal-lattice parameters for SnO_2 (Point group: 4/m 2/m 2/m; Latice parameters: a = 4.737 Å, c = 3.185 Å, α = 90°, β = 90°, γ = 90°), Fe (Lattice structure: body-centered cubic (BCC); Lattice constant: 2.870 Å) and Si (diamond lattice structure that Ashcroft and Mermin call "two interpenetrating face-centered cubic" primitive lattices, where the cube side for silicon is 5.43 Å) [17–21]. The average value of the magnetic moment was calculated for non-relaxed system at T = 77 K, assuming that the Fermi-state population distribution in zero field is conserved in presence of a magnetic field. Note that in comparison with the first approach considered above, the second one better reproduces the number of resonance peaks and their relative intensity distribution, as compared to the experimental spectrum.

Typical anticrossing spectra are shown in Fig. 5(I), calculated for the 1D and 3D models. Fig. 5(II) shows for comparison the simulated spectra produced by the phenomenological model.

The calculations presented in Fig. 5(I) only produce the line intensity and line position; line widths were not calculated, as the spin relaxation was disregarded. However, the spectrum of Fig. 5(I) has finite line widths, introduced as phenomenological parameters for better presentation. The calculated spectrum qualitatively reproduces the positions of the experimental lines (see Fig. 5(I). Once more we note the insufficient accuracy of the present numerical approach, excluding quantitative agreement with the experimental spectra. In comparison with the results shown in Fig. 5(I), the simulated spectra shown in Fig. 5(II) are in much better agreement with the experimental exchange resonance spectrum. Good agreement between experimental and simulated spectra shown in Fig. 5(II) was obtained by using the

Table 3
Positions and output magnetic moments (proportional to the line intensity) of the calculated resonance peaks for the SnO_2–Vacuum–Fe–Si four nanolayer sandwich device.

Position, kG	Magnetic moment, μ_B	Position, kG	Magnetic moment, μ_B
6.25	0.71	3.12	1.42
5.86	0.76	2.69	1.65
5.50	0.80	2.24	1.98
4.98	0.89	1.93	2.29
4.67	0.95	1.72	2.57
4.46	0.99	0.89	4.97
4.31	1.03	0.69	6.42
4.20	1.05	0.41	10.80
4.11	1.08	0.40	11.07
4.04	1.10	0.39	11.35
3.51	1.26		

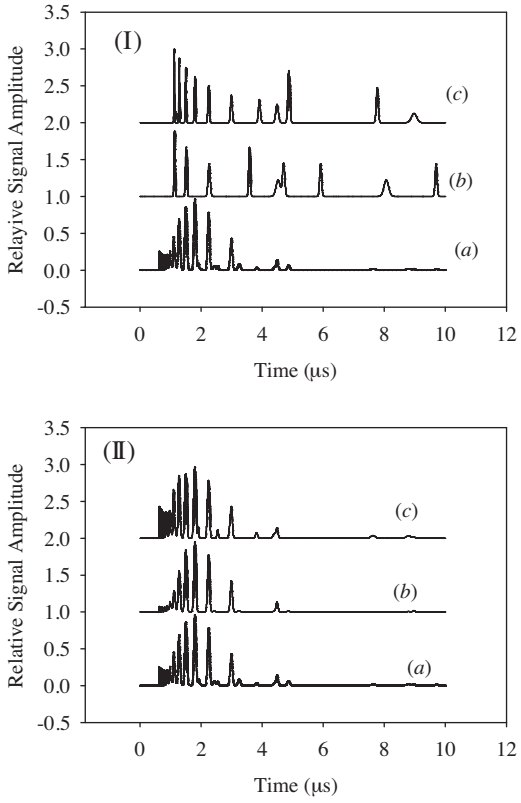

Fig. 5. The magnetic field strength dependence of the magnetic moment averaged over the output surface. (I) The 1D (b) and 3D (c) models were used to simulate the SnO_2–vacuum–Fe–Si device at 77 K; (*a*) experimental spectrum of the SnO_2 (h_{S1} = 8.0 nm) + SiO_2 (h_d = 8.1 nm) + Fe (h_{Fe} = 7.9 nm) + Si (h_{S2} = 8.4 nm) sandwich device. (II) The spectral components of Fig. 2 are described by the phenomenological parameters listed in Table 2: (b) superposition of the fitted spectral components with 1: 0.7: 0.3: 0.5 weights; (c) superposition of the fitted spectral components with 0.8: 0.7: 1: 0.6 weights; (a) experimental spectrum of the same sandwich device.

phenomenological model [10–12], with model parameter values obtained by fitting the model to the experimental spectra.

The magnetic properties of different materials have been extensively studied earlier using the *ab initio* approach [15–17,21–28]. However, there are no publications discussing systems similar to those presently studied. In the present study, we used the previously proposed numerical methods [21,26] that we modified by adding the Zeeman interaction term. The state anticrossing effect was created by the exchange interaction between the Zeeman substates with coincident M_S and S values, where S is the total system spin angular momentum and M_S its projection on the field direction. Note that the spectra calculated in both the 3D and 1D models reproduce the experimental spectrum with a similar level of accuracy. Recalling that the experimental device used the needle tip 50 μm in diameter, a better model should consider interactions between three disks 50 μm in diameter and 8 nm thick. Presently, it is not possible to do *ab initio* calculations for such a large system. An alternative approach that we shall pursue involves representing the nanolayers as continuous media, with the electrons moving within certain potentials. We also disregarded hyperfine interactions, which result in the quantization of the total angular momentum $F = S + L + I$, as the accuracy of our experimental and calculation methods was insufficient for the hyperfine structure to be resolved. This issue will be addressed in a future study.

5. Conclusions

The proposed novel spintronic device operates on magnetic moments of the electronic spin states in different nanolayers. Our phenomenological model assumes that the spin state gets transferred from one layer to another, detached from the respective electrons, which cannot be transported through a dielectric layer. The strength of the interaction inducing spin-polarized state transport is controlled by the thickness of the dielectric layer. We predict that oscillations (the observed exchange–resonance peaks) of the magnetic field strength may be created in the device, provided a sufficiently fast external magnetic field pulse is applied. The spin-polarized spectrum generated by the device consists of S discrete bands, where S is the total spin angular momentum of the Fe–Si layer coupled by the exchange interaction to another semiconductor layer. The proposed model was partially verified in the experiments [10]. Presently, we tested new devices with SDIS structure, using SnO_2 as the first semiconductor nanolayer. The output signal of the SDIS devices is different from that of the previously studied devices [10]. Our phenomenological model was used to fit the experimental spectra, achieving good agreement with experimental results. The fitting procedure produced estimates of the model parameters; their physical interpretation and possible mechanisms involved have been discussed earlier [10]. *Ab initio* analysis of the four-nanolayer devices demonstrated that magnetic field dependence of the output signal averaged over the surface has resonance structure. Presently, such methods are unable to provide the accuracy needed to reproduce the detailed structure of the experimental spectrum, producing only a qualitative agreement. We may expect that increasing of number of atoms in modeling system will increase accuracy and will give better agreement between experimental and *ab initio* theoretical spectra.

Acknowledgement

V.M. is very grateful for financial support from DoE Grant #DE-F602-o8ER46526.

References

[1] C. Kittel, Introduction to Solid State Physics, WSE, Wiley, New York, 1973.
[2] R.A. Serota , arXiv:cond-mat /0007297v1, 18 Jul 2000.
[3] V.A. Koziy , M.A. Skvortsov , arXiv:1106 .3863v1, 20 Jun 2011.
[4] E. Hofstetter , M. Schreiber , arXiv:cond-mat /9408040v1, 12 Aug 1994.
[5] K.R. Barqawi, Z. Murtaza, T.J. Meyer, J. Phys. Chem. 95 (1991) 47.
[6] X.-F.F. Wang, Z. Wang, G. Kotliar, Phys. Rev. Lett. 68 (1992) 2504.
[7] W. Hubner, K. H. Bennemann, arXiv:cond-mat/9508120v1, 25Aug1995.
[8] R.E. George, W. Witzel, H. Riemann, N.V. Abrosimov, N. Notzel, M.L.W. Thewalt, J.J.L. Morton, Phys. Rev. Lett. 105 (2010) 067601.
[9] V.P. Zhukov, E.V. Chulkov, P.M. Echenique, Phys. Stat. Sol. A 205 (1296) (2008) .
[10] V.I. Makarov, S.A. Kochubei, I. Khmelinskii, J Appl. Phys. 110 (2011) 063717.
[11] V.I. Makarov, I. Khmelinskii, arXiv: 1405 .5243, 13 May 2014, http://arxiv.org/ftp/arxiv/papers/1405/1405.5243.pdf, visited: September 2014.
[12] V.I. Makarov, I. Khmelinskii, arXiv: 1405. 4889, 13 May 2014; http://arxiv.org/ftp/arxiv/papers/1405/1405.4889.pdf, visited: September 2014.
[13] R.P. Feynman Statistical Mechanics. California Institute of Technology, W.A. Benjamin Inc. Advanced Book Program, Reading, Massachusets 1972.
[14] E.M. Lifshic, L.P. Pitaevskii, Physical Kinetics, 9th Ed., Butterworth Heinemann, Oxford, Boston Johannesburg, 1997.
[15] C. Kittel, Quantum Theory of Solids Department of Physics, University of Berkley, John Wiley & Sons Inc., California, New York–London, 1963, pp. 64–92.
[16] A. Carrington, A.D. McLachlan, Introduction to Magnetic Resonance, Harper&Row Publisher, 1967, 2014.
[17] D. Li, Y. Gu, Z. Nie, B. Wang, H. Yan, J. Mater. Sci. Technol. 22 (2006) 833.
[18] M.F. Islam, C.M. Canali, Phys. Rev. 85 (2012) 155306.
[19] X. Qian, F. Wagner, M. Peterson, W. Hubner, J. Magn. Magn. Mater. 213 (2000) 12.
[20] Ya Kouji, S. Kunio, O. Toru, Metall. Mater. Trans. B 42 (2010) 37.
[21] Web elements: Platinum crystal structure, http://www.webelements.com/platinum/crystal_structure.html, visited: September 2014.
[22] A.B.D. Nandiyanto, S.-G. Kim, F. Iskandar, K. Okuyama, Micropor. Mesopor. Mater. 120 (2009) 447.
[23] http://www.rocksclusters.org/rocks-documentation/4.1/getting-started.html.
[24] A. Gonzalez-Garcia, W. Lopez-Perez, R. Gonzalez-Hernandez, Computat. Mater. Sci. 55 (2012) 171.
[25] M. Černý, J. Pokluda, M. Šob, M. Friák, P. Šandera, Phys. Rev. B 67 (2003) 035116.
[26] J. Wang, J.-M. Albina, Y. Umeno, J. Phys.: Condens. Matter 24 (245) (2012) 501.
[27] G. Lopez Laurrabaqio, M. Perez Alvarez, J.M. Montejano-Carrizales, F. Aguilera-Grania, J.L. Moran-Lopez, Revista Mexicana de Fisica 52 (2006) 329.
[28] M. Werwinski , A. Szajek , P. Lesniak , W.L. Malinowski , M. Stasiak , Proceeding of the European Conference Physics of Magnetism, (PM11) Poznan, June 27–July 1, 2011.